The Astrophysical Journal, 965:67 (15pp), 2024 April 10 https://doi.org/10.3847/1538-4357/ad2fc0
© 2024. The Author(s). Published by the American Astronomical Society.
OPEN ACCESS

The High-mass X-Ray Binary Luminosity Functions of Dwarf Galaxies

Robel Geda[1], Andy D. Goulding[1], Bret D. Lehmer[2], Jenny E. Greene[1], and Anish Kulkarni[3]
[1] Department of Astrophysical Sciences, Princeton University, Princeton, NJ 08540, USA
[2] Department of Physics, University of Arkansas, 226 Physics Building, 825 West Dickson Street, Fayetteville, AR 72701, USA
[3] Department of Physics, Princeton University, Princeton, NJ 08540, USA
Received 2023 August 24; revised 2024 January 23; accepted 2024 February 23; published 2024 April 8

Abstract

Drawing from the Chandra archive and using a carefully selected set of nearby dwarf galaxies, we present a calibrated high-mass X-ray binary (HMXB) luminosity function in the low-mass galaxy regime and search for an already hinted at dependence on metallicity. Our study introduces a new sample of local dwarf galaxies ($D < 12.5$ Mpc and $M_* < 5 \times 10^9\,M_\odot$), expanding the specific star formation rates (sSFR) and gas-phase metallicities probed in previous investigations. Our analysis of the observed X-ray luminosity function indicates a shallower power-law slope for the dwarf galaxy HMXB population. In our study, we focus on dwarf galaxies that are more representative in terms of sSFR compared to prior work. In this regime, the HMXB luminosity function exhibits significant stochastic sampling at high luminosities. This likely accounts for the pronounced scatter observed in the galaxy-integrated HMXB population's L_X/SFR versus metallicity for our galaxy sample. Our calibration is necessary to understand the active galactic nuclei content of low-mass galaxies identified in current and future X-ray survey fields and has implications for binary population synthesis models, as well as X-ray-driven cosmic heating in the early Universe.

Unified Astronomy Thesaurus concepts: High mass x-ray binary stars (733); Metallicity (1031); Star formation (1569); Dwarf galaxies (416); X-ray binary stars (1811); X-ray astronomy (1810); Compact objects (288)

Supporting material: machine-readable table

1. Introduction

High-mass X-ray binaries (HMXBs) are binary systems that consist of a compact object, a black hole or neutron star, that is accreting material from a high-mass companion star ($M_* > 10\,M_\odot$). Because of the relatively short lifetimes of the high-mass stars in HMXBs, the total X-ray luminosity of HMXBs serves as a powerful tool for probing star formation rates (SFRs) in galaxies (e.g., Hornschemeier et al. 2000; Grimm et al. 2003; Ranalli et al. 2003; Persic et al. 2004; Lehmer et al. 2010, 2016; Mineo et al. 2012; Basu-Zych et al. 2013; Fornasini et al. 2018; Saxena et al. 2021). In addition, there is growing evidence suggesting that HMXBs in dwarf galaxies in the early Universe may have contributed significantly to the ionizing radiation during the preheating of the intergalactic medium leading up to the epoch of reionization (Warszawski et al. 2009; Madau & Fragos 2017; Eide et al. 2018). The study of HMXBs also provides an important constraint on binary star and compact object evolution, with important implications for gravitational wave sources (Podsiadlowski et al. 2003; Abbott et al. 2016; Liotine et al. 2023).

For galaxies that are actively forming stars, the HMXB X-ray luminosity function has been observed to predominantly correlate with the overall SFR of the host galaxy as expected (Grimm et al. 2003; Gilfanov 2004; Mineo et al. 2012; Lehmer et al. 2019, L19 hereafter). However, recent observations and theoretical work suggest that the HMXB luminosity function may also depend on factors such as metallicity and star formation history (SFH). Various models have been proposed to describe the dependence of the luminosity function on metallicity (Brorby et al. 2014; Basu-Zych et al. 2016; Ponnada et al. 2020), primarily interpreting the L_X/SFR versus metallicity relation. Lehmer et al. (2021, L21 hereafter), in particular, observe that this metallicity dependence causes an excess of sources above 10^{38} erg s^{-1} for low-metallicity galaxies and introduce a framework for modeling the HMXB X-ray luminosity functions as a function of SFR and metallicity.

Thanks to their low metallicities (Tremonti et al. 2004; Mannucci et al. 2010), dwarf galaxies serve as a valuable tool to examine the impact of low-metallicity environments on the HMXB X-ray luminosity function. In dwarf galaxies, another consideration becomes highly relevant. HMXBs are the dominant contributors to the overall X-ray luminosity of any star-forming galaxy without an active galactic nucleus (AGN). In dwarf galaxies, however, the contribution of HMXBs may dominate over that of an active nucleus as well since dwarf galaxies may harbor very low-mass central black holes (Mezcua 2017; Greene et al. 2020). The X-ray emission from HMXBs becomes a dominant source of confusion in the context of intermediate-mass black hole detection in distant dwarf galaxies, where we cannot resolve individual HMXBs with current telescopes (Schramm et al. 2013; Pardo et al. 2016; Mezcua et al. 2018; Halevi et al. 2019). Without a better understanding of the full range of L_X per unit of SFR from dwarfs, it is not possible to robustly identify AGN candidates using X-rays; while there is hope to detect and characterize seed black holes in the early Universe using next-generation X-ray missions (Natarajan et al. 2017; Barrow et al. 2018; Ricarte & Natarajan 2018; Haiman et al. 2019). A better handle on the role of metallicity in setting the HMXB luminosity function is urgently needed for this purpose.

In this work, we seek to understand this possible metallicity dependence more fully by increasing the sample of dwarf

Original content from this work may be used under the terms of the Creative Commons Attribution 4.0 licence. Any further distribution of this work must maintain attribution to the author(s) and the title of the work, journal citation and DOI.

galaxies with measured HMXB luminosity functions. Prior studies suggest that local dwarf galaxies exhibit a metallicity-driven surplus of high L_X sources, consequently affecting the shape of their X-ray luminosity functions (Mapelli et al. 2010; Prestwich et al. 2013; Brorby et al. 2014; Douna et al. 2015; Kovlakas et al. 2020). In particular, there appears to be an excess of so-called *ultraluminous X-ray* (ULX) sources in low-mass and low-metallicity galaxies. ULXs are X-ray point sources with luminosities that exceed the Eddington limit for stellar-mass black holes (10^{39} erg s^{-1}). Fully characterizing the HMXB X-ray luminosity function for a larger and more representative sample of dwarf galaxies will quantify whether low metallicity leads to this apparent ULX excess. Further, as shown by Fornasini et al. (2020), the metallicity dependence of L_X/SFR is not expected to evolve with redshift, allowing us to consider local dwarfs as useful analogs for distant dwarf galaxies.

Past studies have often focused on a limited sample of dwarf galaxies, predominantly favoring those with high sSFRs and the lowest known metallicities (Prestwich et al. 2013). L21, in particular, rely on these galaxies to constrain their low-metallicity luminosity functions, but leave a notable gap between 12 + log(O/H) ≈ 7.6–8.0 range as a consequence. We fill this gap by broadening our sample to include a wider metallicity range of 12 + log(O/H) = 7.74–8.77, thus encompassing typical dwarfs with $M_* \sim 10^8$–$10^9\,M_\odot$ and log sSFR ∼ − 10.7–8.5. In addition to being targeted by the Chandra X-ray Observatory, these galaxies also benefit from supporting data from the Galaxy Evolution Explorer (GALEX) telescope and Hubble Space Telescope (HST), enabling us to define uniform apertures and obtain reliable measurements of their SFRs.

The structure of this paper is as follows: in Section 2, we discuss our selected sample of galaxies. Section 3 outlines the data preparation for our analysis. The luminosity function models and the results of our fitting are detailed in Sections 4 and 5, respectively. Finally, Section 6 discusses the L_X–SFR–metallicity relation observed in our sample.

2. Galaxy Sample

Here we present the Chandra+HST dwarf sample. We focus on local dwarf galaxies with stellar masses $M_* < 5 \times 10^9\,M_\odot$ from two Local Volume surveys ($D < 12.5$ Mpc; see Figure 1). The Chandra data are used to identify HMXBs, while the HST data ensure high-fidelity mass and distance measurements for the galaxies. Specifically, we start with a primary sample consisting of two large complementary sets of nearby galaxies, the Legacy ExtraGalactic UV Survey (LEGUS; Cignoni et al. 2018; Sacchi et al. 2018; Cignoni et al. 2019) and the STARBurst IRregular Dwarf Survey (STARBIRDS; McQuinn et al. 2015). Both LEGUS and STARBIRDS have sensitive multiband coverage from HST's WFC3, GALEX (Martin et al. 2005), and the Spitzer Space Telescope's IRAC offering full UV to IR coverage of the galaxy spectral energy distributions. Given the high quality of available data for these sources, they each have extremely accurate (1) direct distances derived from the tip of the red giant branch, surface brightness fluctuations, Cepheids, and/or Type II supernovae measurements; (2) M_* measurements using multiband photometry; (3) SFRs from HST+GALEX photometry; and (4) gas-phase metallicity measurements using oxygen abundances obtained from spectroscopic follow-up. We use X-ray data from NASA's Chandra X-ray Observatory, which offers the angular resolution and sensitivity needed to quantify the X-ray binary (XRB) populations in nearby galaxies. Among the 52 galaxies in the STARBIRDS and LEGUS data sets with stellar masses $M_* < 5 \times 10^9\,M_\odot$, 30 (58%) of these galaxies have publicly available data from Chandra. These observations were taken using the Advanced CCD Imaging Spectrometer (ACIS) from either I (Imaging) or S (Spectroscopy) cameras. Specifically, we label the sample of galaxies that have Chandra ACIS-I/S data as the Chandra+HST sample.

The stellar masses for the Chandra+HST sample were measured by Calzetti et al. (2015) and McQuinn et al. (2010) for the LEGUS and STARBIRDS subsamples, respectively. Calzetti et al. (2015) obtain stellar masses from extinction-corrected *B*-band luminosities and color information, using the method described in Bothwell et al. (2009) and based on the mass-to-light ratio models from Bell & de Jong (2001). McQuinn et al. (2010) calculate the total amount of stellar mass from published absolute *B*-band luminosities of the galaxies, adjusted for extinction from Galactic dust maps published by Schlegel et al. (1998). We use metallicities compiled by Calzetti et al. (2015) based on direct temperature measurements in the literature. For the Chandra+HST sample, we use distances reported by Lee et al. (2009). Galaxies in the Chandra +HST sample span a mass range of log $(M_*/M_\odot) = 6.8 - 9.5$ and a distance range of 0.5–12.5 Mpc.

Although 30 galaxies in LEGUS+STARBIRDS have Chandra data, not all of them have sufficient data for our purposes. We remove two galaxies that were only observed with a sub-array, which is unable to cover the full extent of our nearby galaxies. We then remove an additional six galaxies because they do not reach our required depth of $\log L(\mathrm{erg\ s^{-1}}) > 37.5$ (see Section 3.4 for details).

The rejected galaxies and the reasons that they were rejected are indicated by flags in the Flag column of Table 1. The total number of Chandra+HST dwarf galaxies in the sample after all cuts is 22.

2.1. Additional Dwarfs from L21

In addition to our primary sample, after applying our mass ($M_* < 5 \times 10^9\ M_\odot$) and distance ($D < 12.5$ Mpc) cuts, we obtained 11 local dwarfs from the L21 main sample that are not in the Chandra+HST sample. We identified six additional dwarf galaxies (UGC 05340, NGC 1705, NGC 1569, NGC 5253, NGC 5474, and NGC 7793) that are in both L21 and Chandra+HST. We list the overlapping galaxies under the Chandra+HST category to avoid duplication. For these galaxies, we use X-ray photometry and distances from L21 to preserve the X-ray luminosities reported in that work, and any other galaxy properties from measurements made for the Chandra+HST sample (see Section 3).

The galaxies in the original L21 main sample span a mass range of log $(M_*/M_\odot) = 7.3$–10.4 and a distance range of 1.9–29.4 Mpc. The metallicities of galaxies in the L21 sample were derived using oxygen abundance measurements either from strong-line calibrations or direct electron-temperature-based theoretical calibration (L21). It is worth noting that for objects in common between the two samples, the metallicities are in good agreement despite being derived from different sources.

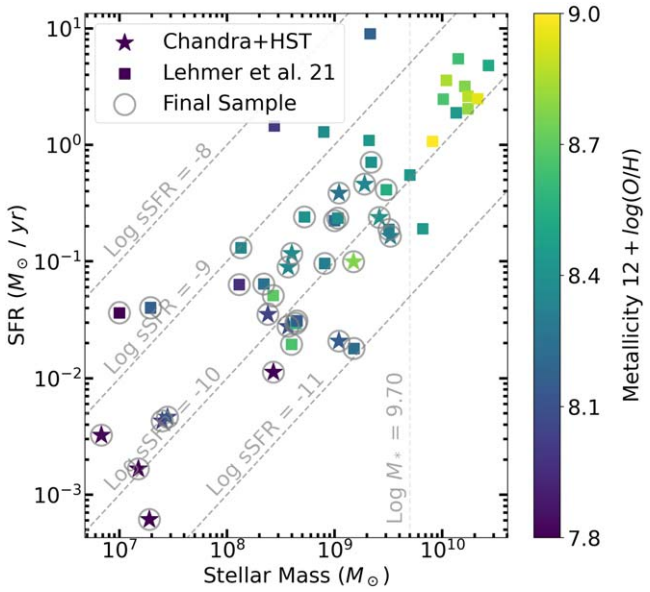

Figure 1. Stellar mass vs. SFR for the galaxies in the L21 galaxy sample and galaxies introduced in this study ("Chandra+HST"). Chandra+HST are reprinted by stars, while L21 galaxies are marked by square points. The points are colored according to gas-phase metallicity (12 + log(O/H)). Our dwarf galaxy sample supplements the L21 sample in M_*, SFR, and metallicity while maintaining a comparable sSFR. The gray circles denote galaxies that satisfy the mass ($M_* < 5 \times 10^9\ M_\odot$) and distance ($D < 12$ Mpc) requirements (in both samples), mainly set by limits in STARBIRDS and LEGUS from which our sample is drawn from. The diagonal gray lines show log sSFRs, and the vertical line denotes our mass cutoff limit.

2.2. ULX Galaxies

Our goal is an unbiased dwarf sample to study X-ray point-source distributions. If galaxies were preferentially targeted by Chandra because of known bright X-ray point sources (i.e., ULXs), this could bias the number of detected sources at the bright end of the luminosity function. Many galaxies in the sample were targeted because of the known presence of a ULX. Specifically, we find that four galaxies—NGC 7793, NGC 4490, NGC 4485, and NGC 1313—were targeted for ULXs. Therefore, we fit the X-ray luminosity functions with and without the ULX-targeted sample to assess the potential bias introduced by their addition.

2.3. Summary of Final Sample

We have identified a total of 33 individual galaxies that meet our criteria, 22 from Chandra+HST and 11 from L21. We will refer to this set of galaxies as our final sample. However, we further perform our analysis with and without the four galaxies targeted because they harbor ULXs. The sample containing ULX galaxies will be referred to as the "final+ULX" sample. The galaxies in the final sample span a stellar mass range of $\log(M_*/M_\odot) = 6.8$–9.52, gas-phase metallicity range of $12 + \log(\mathrm{O/H}) = 7.74$–$8.77$, and a distance range of 0.5–12.1 Mpc.

3. Data Analysis

In this section, we discuss galaxy apertures (Section 3.1), SFR measurements (Section 3.2), X-ray photometry (Section 3.3), and recovery (completeness) functions (Section 3.4) used in this study. We compute galaxy sizes and recovery functions, and perform X-ray photometry for all galaxies in the Chandra+HST sample (i.e., before final sample selection), while utilizing published X-ray catalogs from L21 for galaxies covered in that study. We compute galaxy sizes and associated far-ultraviolet (FUV) SFRs for galaxies in the final sample. Table 2 presents X-ray and SFR measurements for galaxies that met all of our selection criteria (i.e., final sample+ULX).

3.1. Galaxy Apertures Using GALEX

We use galaxy-projected footprints as apertures when making photometric measurements and as boundaries when filtering for X-ray point sources. L21 uses apertures defined by the Two Micron All Sky Survey (2MASS; Jarrett et al. 2003) 20 mag arcsec^{-2} isophotal ellipses in the K_s band. However, several dwarf galaxies in this study are fainter in the K_s band than the L21 sample because they are relatively blue, causing the 2MASS K_s-band apertures to severely underestimate the sizes of those galaxies, and therefore underestimate the number of HMXBs within them. Taking this into account, we use elliptical apertures from GALEX as a basis to define the projected apertures of galaxies in this study.

In their study, Lee et al. (2009) define the semimajor and semiminor axes of the outermost elliptical annulus for each galaxy from the GALEX photometry. This boundary is determined based on two criteria: it is either the point where the annular flux error exceeds 0.8 mag or the point where the intensity drops below the level of the sky background. We performed aperture photometry on the GALEX data using full-sized, half-sized, and quarter-sized versions of the apertures reported by Lee et al. (2009). We found that the half-sized apertures minimized cosmic X-ray background (CXB) contamination, closely matched the effective radius of most galaxies in our sample, and that they are similar to the apertures used in L21. We, therefore, adopt the half-sized apertures as our galaxy footprints.

NGC 5408 and ESO 495-G021 (He2-10) have no available UV observations with GALEX. We use the 2MASS apertures provided in L21 since these galaxies are sufficiently bright in the K_s band (9.00 and 11.39 mag, respectively, Skrutskie et al. 2006). The positions and X-ray photometry for sources within and surrounding the L21 apertures are presented in Table A1 in L21. To identify sources that fall within our galaxy aperture, we apply a positional filter on the point sources flagged in the table in L21 as 1, 3, and 5, which correspond to point sources within the L21 aperture, sources outside the L21 aperture, and sources that are beyond 1.2 times the galaxy boundaries, respectively. We report our adopted apertures in Table 1 and display the apertures of Chandra+HST galaxies in Figure 2 (magenta ellipses).

3.2. SFRs

To ensure consistency and take into account the new apertures discussed in Section 3.1, we recalculate the FUV-derived SFRs of each galaxy using GALEX data. To achieve this, we measure the total flux enclosed within our FUV galaxy apertures and correct for Milky Way foreground extinction using $E(B-V)$ colors from Schlegel et al. (1998; as reported in Lee et al. 2009). The FUV fluxes are then converted to luminosities using the distance to the galaxy, which in turn is used to measure the SFR. We expect internal FUV extinction in the dwarf galaxies to be small because our combined sample is

Table 1
Chandra+HST Sample before Selection and Selected L21 Dwarfs[a]

Name	α_{J2000} R.A.	δ_{J2000} Decl.	$E(B-V)$	D (Mpc)	a (arcmin)	b (arcmin)	PA (deg)	M ($M_\odot$)	12+log[O/H] (mag)	FUV (mag)	Flag	Source
(1)	(2)	(3)	(4)	(5)	(6)	(7)	(8)	(9)	(10)	(11)	(12)	(13)
NGC 0045	$00^h14^m04\overset{s}{.}0$	$-23°10'55\overset{''}{.}0$	0.02	7.1	3.15	2.18	−38	9.52	8.31	13.18 ± 0.08	⋯	LG
NGC 0625	$01^h35\ 04\overset{s}{.}2$	$-41°26'15\overset{''}{.}0$	0.02	4.1	1.43	0.47	−88	8.57	8.10	13.90 ± 0.12	⋯	SB
IC 1727	$01^h47\ 30\overset{s}{.}6$	$+27°19'52\overset{''}{.}0$	0.08	7.2	1.27	0.57	−30	8.74	8.73	⋯	RF	LG
NGC 1313	$03^h18\ 15.8$	$-66°29'53\overset{''}{.}0$	0.11	4.2	2.15	1.63	+40	9.41	8.40	11.61 ± 0.06	⋯	LG
NGC 1569	$04^h30^m49\overset{s}{.}0$	$+64°50'53\overset{''}{.}0$	0.69	1.9	1.10	0.55	−60	9.00	8.19	9.98 ± 0.20	⋯	SB+L21
NGC 1705	$04^h54^m13\overset{s}{.}7$	$-53°21'41\overset{''}{.}0$	0.01	5.1	0.57	0.42	+50	8.11	7.96	13.50 ± 0.09	⋯	LG+L21
NGC 2500	$08^h01^m53\overset{s}{.}3$	$+50°44'15\overset{''}{.}0$	0.04	7.6	0.88	0.78	0	9.28	8.84	⋯	RF	LG
UGC 04459	$08^h34\ 07\overset{s}{.}2$	$+66°10'54\overset{''}{.}0$	0.04	3.6	0.45	0.39	−60	6.83	7.82	15.94 ± 0.29	⋯	LG
UGC 04483	$08^h37^m03\overset{s}{.}0$	$+69°46'31\overset{''}{.}0$	0.03	3.2	0.33	0.24	−18	7.18	7.50	16.44 ± 0.35	⋯	SB
Holmberg I	$09^h40^m32\overset{s}{.}3$	$+71°10'56\overset{''}{.}0$	0.05	3.8	1.02	0.85	0	7.40	8.00	15.80 ± 0.30	⋯	LG
UGC 05340	$09^h56^m45\overset{s}{.}7$	$+28°49'35\overset{''}{.}0$	0.02	12.1	0.80	0.30	0	7.00	7.20	15.97 ± 0.28	⋯	LG+L21
NGC 3274	$10^h32^m17\overset{s}{.}1$	$+27°40'07\overset{''}{.}0$	0.02	6.5	1.02	0.49	−80	8.04	8.33	⋯	RF	LG
UGC 06456	$11^h28^m00\overset{s}{.}0$	$+78°59'39\overset{''}{.}0$	0.04	4.3	0.42	0.24	−10	7.83	7.64	⋯	SA	SB
NGC 3738	$11^h35^m48\overset{s}{.}8$	$+54°31'26\overset{''}{.}0$	0.01	4.9	0.45	0.34	−25	8.38	8.04	14.04 ± 0.12	⋯	LG
NGC 4214	$12^h15^m38\overset{s}{.}9$	$+36°19'40\overset{''}{.}0$	0.02	2.9	2.10	1.63	−40	8.60	8.38	11.62 ± 0.04	⋯	SB
NGC 4242	$12^h17^m30\overset{s}{.}1$	$+45°37'08\overset{''}{.}0$	0.01	7.4	0.92	0.70	+25	9.04	8.15	15.51 ± 0.23	⋯	LG
NGC 4395	$12^h25^m48\overset{s}{.}9$	$+33°32'48\overset{''}{.}0$	0.02	4.6	2.45	2.04	−33	8.77	8.26	⋯	SA	LG
UGCA 281	$12^h26^m16\overset{s}{.}0$	$+48°29'37\overset{''}{.}0$	0.01	5.7	0.28	0.21	−85	7.28	7.82	15.53 ± 0.22	RF	LG
NGC 4449	$12^h28\ 11\overset{s}{.}2$	$+44°05'36\overset{''}{.}0$	0.02	4.2	1.93	1.37	+45	9.04	8.26	11.12 ± 0.03	⋯	LG
NGC 4485	$12^h30^m31\overset{s}{.}1$	$+41°42'01\overset{''}{.}0$	0.02	7.1	0.85	0.59	+15	8.57	8.36	13.84 ± 0.11	⋯	LG
NGC 4490	$12^h30^m36\overset{s}{.}1$	$+41°38'34\overset{''}{.}0$	0.02	8.0	1.95	0.96	−55	9.28	8.35	12.32 ± 0.06	⋯	LG
NGC 4605	$12^h40^m00\overset{s}{.}3$	$+61°36'29\overset{''}{.}0$	0.01	5.5	2.45	0.93	−55	9.18	8.77	13.16 ± 0.08	⋯	LG
UGC 08201	$13^h06^m24\overset{s}{.}8$	$+67°42'25\overset{''}{.}0$	0.02	4.6	1.02	0.56	+90	8.43	7.80	15.13 ± 0.20	⋯	SB
NGC 5253	$13^h39^m55\overset{s}{.}9$	$-31°38'24\overset{''}{.}0$	0.06	3.1	1.55	0.59	+45	8.34	8.25	12.44 ± 0.07	⋯	LG+L21
NGC 5474	$14^h05^m01\overset{s}{.}5$	$+53°39'45\overset{''}{.}0$	0.01	6.8	1.43	1.27	0	8.91	8.31	13.67 ± 0.10	⋯	LG+L21
UGC 09128	$14^h15^m56\overset{s}{.}5$	$+23°03'19\overset{''}{.}0$	0.02	2.2	0.50	0.38	+45	7.28	7.74	16.74 ± 0.38	⋯	SB
NGC 5949	$15^h28^m00\overset{s}{.}7$	$+64°45'47\overset{''}{.}0$	0.02	8.5	0.68	0.31	−33	9.26	8.37	⋯	RF	LG
NGC 6503	$17^h49^m27\overset{s}{.}1$	$+70°08'40\overset{''}{.}0$	0.03	5.3	2.20	0.74	−57	9.28	8.51	13.64 ± 0.11	RF	LG
NGC 6822	$19^h44^m56\overset{s}{.}6$	$-14°47'21\overset{''}{.}0$	0.23	0.5	3.82	3.33	0	7.45	8.11	11.29 ± 0.09	⋯	SB
NGC 7793	$23^h57^m49\overset{s}{.}7$	$-32°35'30\overset{''}{.}0$	0.02	3.9	2.58	1.74	−82	9.51	8.31	11.74 ± 0.05	⋯	LG+L21
NGC 0024	$00^h09^m56\overset{s}{.}7$	$-24°57'44\overset{''}{.}0$	0.02	7.3	1.07	0.24	+46	8.64	8.59	15.10 ± 0.20	⋯	L21
MESSIER 074	$01^h36^m41\overset{s}{.}7$	$+15°46'59\overset{''}{.}0$	0.07	7.3	3.25	2.94	+25	9.48	8.54	12.24 ± 0.07	⋯	L21
NGC 0925	$02^h27^m16\overset{s}{.}9$	$+33°34'45\overset{''}{.}0$	0.08	9.1	1.90	1.07	−78	9.03	8.38	13.33 ± 0.12	⋯	L21
ESO 495- G021	$08^h36^m15\overset{s}{.}2$	$-26°24'33\overset{''}{.}7$	⋯	9.0	0.89	0.80	+140	8.72	8.40	⋯	⋯	L21
NGC 2915	$09^h26^m11\overset{s}{.}5$	$-76°37'36\overset{''}{.}0$	0.27	3.8	0.57	0.30	−51	8.65	8.15	13.62 ± 0.25	⋯	L21
NGC 2976	$09^h47^m15\overset{s}{.}3$	$+67°55'00\overset{''}{.}0$	0.07	3.6	1.10	0.50	−37	8.60	8.66	13.99 ± 0.15	⋯	L21
NGC 3125	$10^h06^m33\overset{s}{.}6$	$-29°56'09\overset{''}{.}0$	0.08	12.0	0.53	0.33	−66	8.13	8.34	14.57 ± 0.19	⋯	L21
IC 2574	$10^h28^m21\overset{s}{.}2$	$+68°24'43\overset{''}{.}0$	0.04	4.0	2.45	1.00	+50	9.18	8.23	14.34 ± 0.16	⋯	L21
NGC 4559	$12^h35^m57\overset{s}{.}7$	$+27°57'35\overset{''}{.}1$	0.02	10.3	2.04	0.96	+148	9.34	8.40	12.40 ± 0.06	⋯	L21
NGC 4625	$12^h41^m52\overset{s}{.}6$	$+41°16'26\overset{''}{.}0$	0.02	9.2	1.00	0.86	−30	8.43	8.70	15.02 ± 0.19	⋯	L21
NGC 5408	$14^h03^m20\overset{s}{.}9$	$-41°22'39\overset{''}{.}8$	⋯	4.8	0.75	0.75	+95	7.29	8.17	⋯	⋯	L21

Note. Column (1): galaxy name. Columns (2) and (3): central position R.A. and decl. Column (4): $E(B-V)$ Milky Way extinction. Column (5): distance from Lee et al. (2009) for Chandra dwarfs and Lehmer et al. (2021) for L21 galaxies. Columns (6) and (7): semimajor and semiminor radii of galaxy aperture used in this study. Column (8): position angle of aperture. Column (9): log stellar mass. Column (10): gas-phase metallicity. Column (11): GALEX FUV mag, total flux within galaxy aperture. Column (12): cause of rejection for galaxies that were not included in the analysis where SA is the sub-array mode and RF is the recovery function cutoff. Column (13): source catalog where LG is LEGUS, SB is STARBIRDS, and L21 is Lehmer et al. (2021)

[a] Separated by the horizontal line

Table 2
Our Final Sample[a]

Name	ObsID	Cycle	t (Ks)	ACIS	Log SFR (log yr^{-1})	N	L_X (log erg s^{-1})	L_{CXB} (log erg s^{-1})	L_{LMXB} (log erg s^{-1})	L_{Peak} (log erg s^{-1})	ULX
(1)	(2)	(3)	(4)	(5)	(6)	(7)	(8)	(9)	(10)	(11)	(12)
NGC 0045	4690	5	34.40	S	-0.79 ± 0.032	8	38.51 ± 0.028	38.7	38.6	38.0	No
NGC 0625	4746	5	60.30	S	-1.56 ± 0.047	3	38.35 ± 0.014	37.3	37.7	38.2	No
NGC 1313	2950	3	19.90	S	-0.62 ± 0.024	9	39.57 ± 0.006	37.9	38.5	39.5	Yes
NGC 1569	782	1	95.00	S	-0.65 ± 0.080	12	37.99 ± 0.009	36.6	38.1	37.6	No
NGC 1705	3930	4	56.00	S	-1.20 ± 0.036	1	36.60 ± 0.188	37.0	37.2	36.6	No
UGC 04459	9538	9	25.90	S	-2.49 ± 0.116	0	0.00 ± 0.000	36.5	36.0	0.0	No
UGC 04483	10559	10	3.09	S	-2.78 ± 0.140	0	0.00 ± 0.000	35.9	36.3	0.0	No
Holmberg I	9539	9	25.90	S	-2.37 ± 0.120	3	37.03 ± 0.088	37.3	36.5	36.6	No
UGC 05340	11271	11	118.00	S	-1.44 ± 0.112	2	38.26 ± 0.043	37.8	36.1	38.2	No
NGC 3738	19357	18	9.34	S	-1.45 ± 0.048	0	0.00 ± 0.000	36.7	37.5	0.0	No
NGC 4214	2030	2	26.40	S	-0.93 ± 0.016	15	38.49 ± 0.012	37.6	37.7	38.3	No
NGC 4242	19351	18	9.94	S	-1.68 ± 0.092	0	0.00 ± 0.000	37.7	38.1	0.0	No
NGC 4449	10875	10	59.40	S	-0.41 ± 0.014	24	39.24 ± 0.005	37.9	38.2	38.6	No
NGC 4485	4726	5	39.60	S	-1.05 ± 0.044	4	39.44 ± 0.009	37.6	37.7	39.3	Yes
NGC 4490	4725	5	38.50	S	-0.34 ± 0.024	23	39.98 ± 0.005	38.3	38.4	39.4	Yes
NGC 4605	19344	18	9.67	S	-1.00 ± 0.032	3	38.02 ± 0.081	38.0	38.3	37.7	No
UGC 08201	9537	9	13.50	S	-1.95 ± 0.080	0	0.00 ± 0.000	37.2	37.5	0.0	No
NGC 5253	2032	2	190.00	S	-1.20 ± 0.028	15	38.55 ± 0.007	37.2	37.5	38.4	No
NGC 5474	9546	9	31.00	S	-1.02 ± 0.040	10	38.94 ± 0.022	38.1	38.0	38.6	No
UGC 09128	16121	15	4.91	I	-3.21 ± 0.154	0	0.00 ± 0.000	35.7	36.3	0.0	No
NGC 6822	2925	3	28.10	I	-2.33 ± 0.036	15	36.72 ± 0.018	36.6	36.6	36.3	No
NGC 7793	3954	4	190.00	S	-0.73 ± 0.020	26	38.51 ± 0.009	38.1	38.6	38.2	Yes
NGC 0024	⋯	⋯	43.00	⋯	-1.53 ± 0.078	6	38.03 ± 0.054	37.4	37.8	37.5	No
MESSIER 074	⋯	⋯	268.00	⋯	-0.39 ± 0.028	79	39.43 ± 0.005	39.0	38.6	39.1	No
NGC 0925	⋯	⋯	12.00	⋯	-0.63 ± 0.046	7	39.86 ± 0.017	38.4	38.1	39.6	No
ESO 495- G021	⋯	⋯	216.00	⋯	-0.62	9	38.73 ± 0.014	38.0	37.8	38.4	No
NGC 2915	⋯	⋯	15.00	⋯	-1.51 ± 0.100	0	0.00 ± 0.000	36.6	37.8	0.0	No
NGC 2976	⋯	⋯	9.00	⋯	-1.71 ± 0.058	2	38.80 ± 0.021	37.0	37.7	38.8	No
NGC 3125	⋯	⋯	64.00	⋯	-0.88 ± 0.077	4	39.61 ± 0.012	37.6	37.2	39.5	No
IC 2574	⋯	⋯	11.00	⋯	-1.74 ± 0.063	2	37.76 ± 0.179	37.7	38.3	37.7	No
NGC 4559	⋯	⋯	22.00	⋯	-0.15 ± 0.024	5	40.09 ± 0.009	38.5	38.4	40.0	No
NGC 4625	⋯	⋯	56.00	⋯	-1.30 ± 0.076	7	38.15 ± 0.041	38.1	37.5	37.9	No
NGC 5408	⋯	⋯	70.00	⋯	-1.40	7	39.61 ± 0.004	37.4	36.4	39.6	No

Note. Column (1): galaxy Name. Column (2): Chandra observation ID. Column (3): Chandra observation cycle. Column (4): Chandra exposure time. Column (5): ACIS configuration I for Wide Field Imaging and S for S3 chips. Column (6): log SFR derived from FUV measurement. If FUV information is not available for L21 galaxies, the value from L21 is used. Column (7): number of L_X sources within aperture. Column (8): total point-source L_X. Column (9): total recovery function corrected L_X from the CXB (Kim et al. 2007). Column (10): total, recovery function corrected, L_X expected from LMXB (L19). Column (11): L_X of the most luminous point source within aperture. Column (12): yes, if the galaxy was targeted for ULXs.
[a] L21 dwarfs are separated by the horizontal line.

predominantly comprised of blue dwarf galaxies with negligible dust. We use the scaling relation given by Lee et al. (2009) to convert the FUV luminosity to an SFR of

$$\mathrm{SFR} = 1.4 \cdot 10^{-28} \cdot L_\nu(\mathrm{UV}) \quad (1)$$

where L_ν(UV) is the total FUV luminosity density (erg s^{-1} Hz^{-1}) enclosed. For the two galaxies with no GALEX data, we used the original SFR values from L21.

3.3. X-Ray Photometry and Source Catalogs

The Chandra ACIS data were retrieved from the Chandra archive and homogeneously reprocessed using `chandra_repro` as part of the `CIAO` package v4.14 along with associated calibration files CALDB v4.9.6. As is standard, we applied the latest bad pixel masks and identified afterglow effects to create new masks and applied the very faint processing flag to further clean the particle background for those observations performed in VFAINT mode to create the final reprocessed Level 2 events files and their associated response files. X-ray photometry was further carried out using `CIAO`. We started by constructing images in the 0.5–7.0 keV band from the reprocessed Level 2 events files for the 31 dwarf galaxy candidates in the Chandra +HST sample. For each of the galaxies, we used the `CIAO fluximage` script to create exposure-corrected images using the reprocessed ACIS-graded Level 2 event files in good time intervals along with the associated aspect solution files and bad pixel masks. The point-spread function (PSF) radius was computed using the `mkpsfmap` script with the PSF energy set to 1.4967 keV and the encircled counts fraction set to 0.9. Using the resulting flux image and PSF map as inputs, we ran `wavdetect` with wavelet scales of 1.0, 1.414, 2.0, 2.828, 4.0, 5.657, and 8.0 pixels and `sigthresh` set to 10^{-6}. This step produced our X-ray source photometry (counts) and catalog (positions).

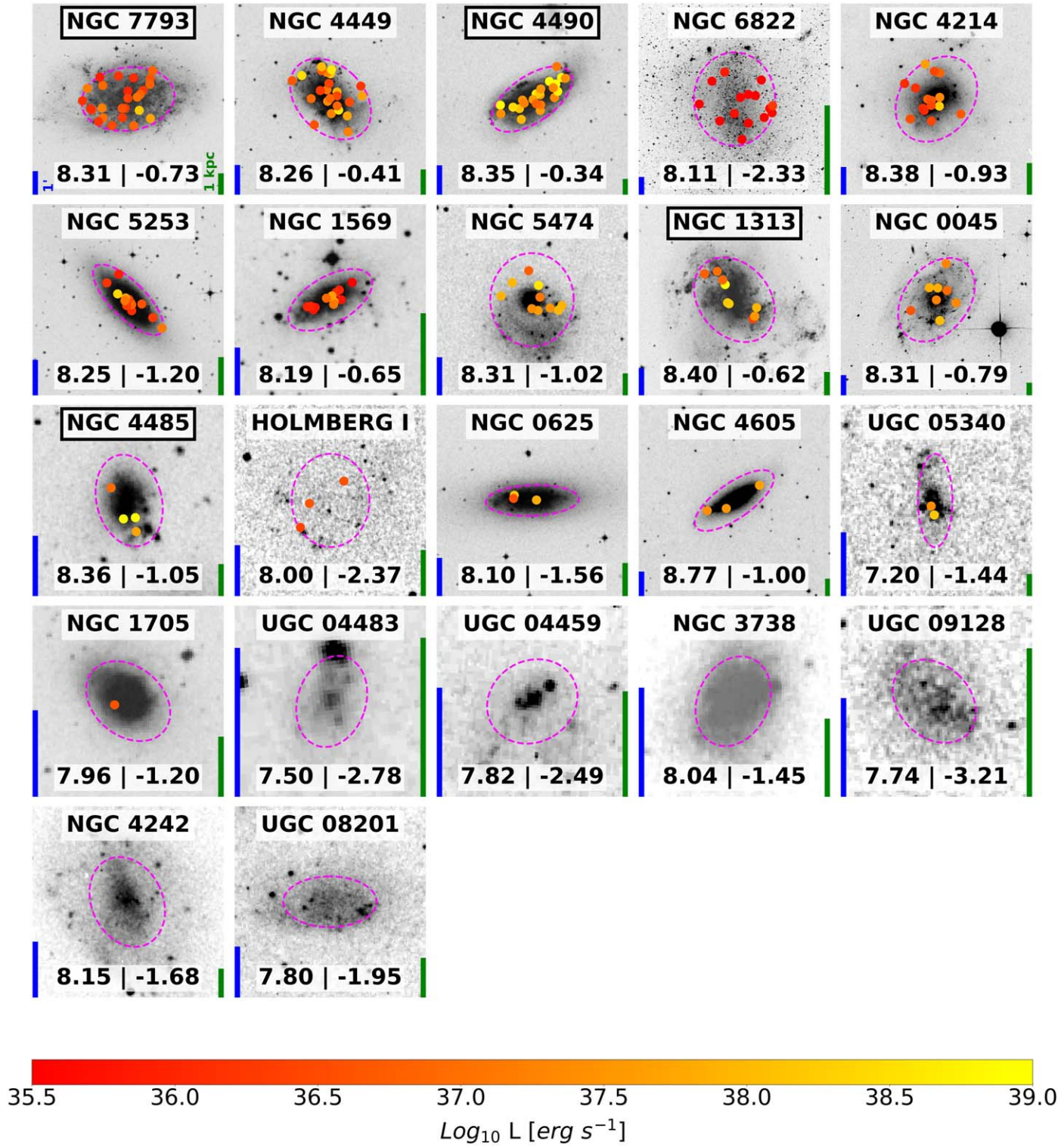

Figure 2. This figure shows the dwarf galaxies in the Chandra+HST final sample. In each panel, we include a Digitized Sky Survey image of the galaxy, which is displayed in grayscale. Galaxy names are displayed at the top of each panel, and the corresponding [12 + log(O/H), log(SFR)] values are displayed at the bottom. If the galaxy was targeted by Chandra for ULXs, the galaxy is noted with a black box around its name. The apertures used in this study are plotted as ellipses (magenta). X-ray sources are overplotted as circles and colored according to their X-ray luminosities. For reference, vertical bars of size 1′ (blue) and 1 kpc at the galaxy's distance (green) are provided in the lower left and lower right corners of each panel, respectively.

For each galaxy, we filter out X-ray sources outside of the ACIS chip and the galaxy's aperture. In particular, for ACIS-S observations we filtered out sources that are not in the same chip as the target galaxy, while for front-illuminated ACIS-I observations, we kept sources within the four chips (including the gaps). We visually inspected each galaxy to identify the presence of X-ray features that we deemed indicative of an AGN at the center of the flux images. UGC 5139, NGC 5253, NGC 4490, NGC 4605, and NGC 2500 were flagged as having possible AGN in the form of an X-ray point source coincident

with their centers. As such, these suspected AGN point sources were filtered out.

We used the PIMMS (Portable, Interactive Multi-Mission Simulator) to calculate the ACIS counts-to-flux conversion factors for each galaxy based on its observation cycle. The input energy range was set to 0.5–7.0 keV for all galaxies. Assuming a power-law spectral model, we set $\Gamma = 1.7$ and estimated the galactic neutral hydrogen column density for each galaxy using the HEASARC software. We then calculated the point-source fluxes by multiplying the counts from `wavdetect` by the conversion factor we obtained from PIMMS. Furthermore, we calculate the 0.5–7.0 keV X-ray point-source luminosities "L" using the distances to the host galaxy.

3.4. Completeness Corrections

The recovery function, denoted by $\xi(L)$, is a statistical measure of the fraction of sources that can be detected at a given X-ray luminosity while addressing source crowding and the galactic backdrop's impact on point-source detection. As such, we compute the recovery function of each galaxy in our sample by simulating a mock image and running our detection algorithm on the simulated data set. We start with the original Chandra data set as a base and use CIAO's `simulate_psf` function to inject 100 additional synthetic sources into the galaxy aperture within the same point-source luminosity bin. `simulate_psf` accounts for streaks and PSF distortions. We run `wavdetect` on the simulated data set and measure $\xi(L)$ as the fraction of the injected sources that we are able to recover. We repeat this for each luminosity bin 10 times (a total of 1000 synthetic sources per luminosity bin per galaxy). We defined $\log L(\mathrm{erg\ s^{-1}}) = 39$ as our maximum recovery function luminosity, while the lower bound is set to one or two bins below the 4 count limit. We sample in intervals of 0.5 dex for luminosities in the range of $\log L(\mathrm{erg\ s^{-1}}) = 37$–$39$ and 0.1 dex for $\log L(\mathrm{erg\ s^{-1}}) < 37$. We use smaller energy bins for $\log L(\mathrm{erg\ s^{-1}}) < 37$ to sufficiently sample the curvature of the recovery function as it begins to fall from unity to zero with decreasing luminosity. The recovery functions of all the galaxies in our sample are displayed in Figure 3.

To ensure the fidelity of our recovery functions, we take the placement of the synthetic sources and the size of each galaxy into consideration. All of the injected point sources are placed such that they are at least one-half PSF radius away from each other, even if they are not injected into the same simulated image. This ensures that no two point sources are probing the same area and reduces the chance of source confusion caused by the synthetic sources overlapping with each other. Note that we do allow synthetic sources to overlap with real sources and incorporate such confusion into the recovery function. Since our sample contains dwarf galaxies, their sizes may be too small to allow for a meaningful measurement of $\xi(L)$. To address this, we set the semimajor and semiminor axes of the galaxy (i.e., our sampling area) to a minimum of 3′. We also restrict the sampling area to be within the ACIS chip projected footprint (except for gaps in ACIS-I images).

4. Modeling

In this section, we discuss forward modeling of the X-ray luminosity functions. Following L19 and L21, we model the observed X-ray luminosity distributions by taking into account the low-end completeness of the observations (Section 4.1), contributions from the CXB (Section 4.2), and high and low-mass binaries (Section 4.3). By modeling each component of the luminosity function separately and combining them into a compound model, we can represent and fit the observed data. The CXB for Chandra has been modeled by Kim et al. (2007), and the completeness of each observation is modeled using simulated recovery functions (see Section 3.4). We find the contributions of LMXBs, which scale with stellar mass, to be negligible for our sample of galaxies and use the L19 LMXB model to represent their magnitude. The last component is the HMXB component, which scales with SFR. We use the Astropy (Astropy Collaboration et al. 2022) `models` subpackage to implement individual and compound models. We describe each model component in detail below.

4.1. Recovery Function Model

We model the fraction of point sources recovered as a function of luminosity L_X (i.e., completeness) using the recovery functions from L21 and the simulated recovery functions in Section 3.4. We implement the model by using the tabulated recovery fractions as look-up tables, interpolating between data points when necessary. For luminosities that correspond to 4 counts or less, we enforce a recovery fraction of 0. For luminosities above the range of the simulated recovery function, we use a recovery fraction of 1.

4.2. CXB

The CXB is the combined X-ray flux from all distant bright X-ray sources, such as AGNs, that may be confused with relatively fewer luminous sources within a nearby galaxy. To model the contribution of such sources, we use the extra-galactic X-ray point-source number counts from Kim et al. (2007). They provide broken power-law models, given in Equation (2), for the ChaMP+CDFs (Rosati et al. 2002; Kim et al. 2004) number counts per unit area, with parameters listed in their publication's Table 4 for each galaxy. We scale this model by the area of our apertures and convert the CXB flux values to luminosities using the distance to the galaxy. To cover the same energy range as our observations, we use the 0.5–8 keV ChaMP+CDFs models. Given a power-law photon index of 1.4, the difference between the 0.5–7 keV and 0.5–8 keV energy ranges is negligible (10%). Our adopted model for the flux (S) dependent CXB number counts can be expressed as

$$\frac{dN_{\mathrm{CXB}}}{dS} = \begin{cases} K\left(\dfrac{S}{S_{\mathrm{ref}}}\right)^{-\gamma_1} & S < S_b \\ K\left(\dfrac{S_b}{S_{\mathrm{ref}}}\right)^{(\gamma_2-\gamma_1)}\left(\dfrac{S}{S_{\mathrm{ref}}}\right)^{-\gamma_2} & S \geqslant S_b \end{cases} \tag{2}$$

where γ_1 and γ_2 are the broken power-law slopes, K is a normalization constant S_{ref} is a normalization flux set to 10^{-15} erg s^{-1}cm^{-2}, and S_b is the break flux at which the slope changes. The differential number count (dN_{CXB}/dS) as stated in Equation (2) is in units of 10^{-15} deg^{-2}.

4.3. LMXB and HMXB Models

We model the LMXB contributions as a function of stellar mass utilizing the L19 broken power-law model (Equation (12)

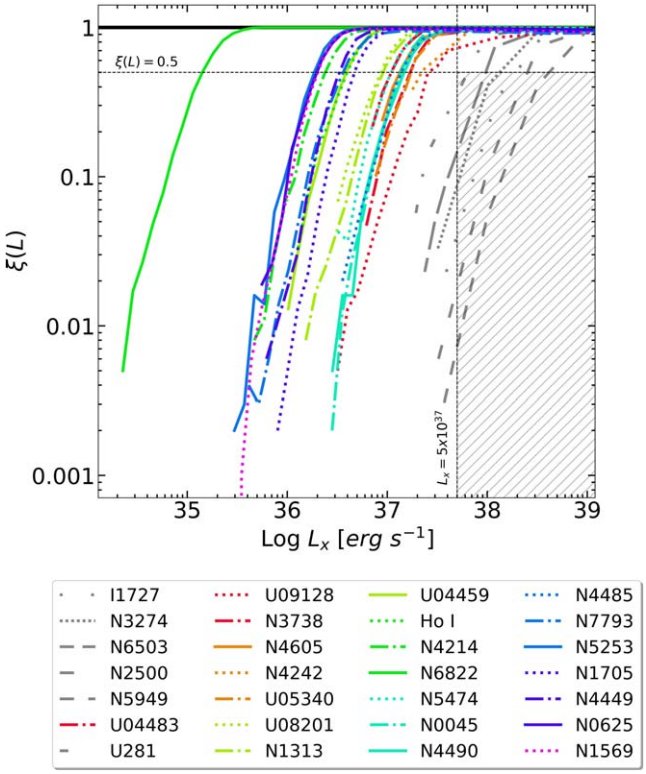

Figure 3. Recovery functions within the apertures of the Chandra+HST sample of galaxies. Sub-array mode galaxies are not included in this figure. Galaxies are colored according to relative exposure times (i.e., by ranking). The Recovery functions were computed by injecting simulated X-ray sources into Chandra images and measuring the fraction of the synthetic sources recovered during the source detection stage. The minimum L_X in the simulations is set by the luminosity, at the galaxy's distance, which corresponds to 4 counts. The gray vertical and horizontal lines denote a log luminosity of 37.5 erg s^{-1} and 50% recovery, respectively. If the $\xi(L)$ profile falls below 50% before 37.5 erg s^{-1}, we do not include that galaxy in our analysis (Recovery functions of rejected galaxies are plotted as gray lines). We note that the recovery function of NGC 6822 extends to relatively lower luminosities despite its exposure time because of its proximity to the Milky Way.

in L19) with a cutoff luminosity. We use parameter values obtained by the L19 full sample (Table 4, column (4) of L19). We do not fit any parameters for the LMXB at any point because the contributions from LMXBs are negligible.

There are two models available for the HMXB. The first model is an SFR-normalized single power-law model from L19, with a cutoff luminosity. The L19 HMXB differential number counts as a function of X-ray luminosity has the following form:

$$B(L) = K_{\mathrm{HMXB,38}} \begin{matrix} L_{38}^{-\gamma} & L < L_c \\ 0 & L \geqslant L_c \end{matrix} \quad (3)$$

$$\frac{dN_{\mathrm{HMXB}}}{dL} = \mathrm{SFR} \cdot B(L) \quad (4)$$

where SFR is the host galaxy star formation rate, K_{HMXB} is a normalizing constant, and γ is the power-law slope. Following L19, we take L to be in units of 10^{38} erg s^{-1} (denoted by $L_{38} = L/10^{38}$) for the HMXB and LMXB models. The only component that varies across galaxies in this model is the SFR, with $B(L)$ being universal for all galaxies in a given metallicity bin.

The L21 HMXB model introduces a metallicity dependence to the differential number counts (Equations (1)–(3) in L21). The function has the form of a broken power law with an exponential cutoff. The high-luminosity power-law exponent, as well as the cutoff luminosity, have metallicity dependencies. When we include the L21 model for comparison, we do not refit any parameters but use the values reported in Table 2 of L21.

4.4. Compound Model

Following L19 and L21, we combine all the elements described above to forward model the underlying HMXB luminosity function (Equation (4)) implied by the ensemble measured luminosity distributions, accounting for incompleteness, CXB, and the LMXB population. The underlying HMXB luminosity function is weighted by the SFR of each galaxy contributing to the ensemble. To account for completeness, the contribution of each galaxy is weighted by its recovery function at each luminosity. This provides us with a model that represents the observed total number counts in each L_X bin (Δn):

$$\Delta n = \sum_i^{N_{\mathrm{gal}}} \xi_i(L) \Delta L \left[\frac{dN_{\mathrm{HMXB},i}}{dL} + \frac{dN_{\mathrm{LMXB},i}}{dL} + \frac{dN_{\mathrm{CXB},i}}{dL} \right] \quad (5)$$

Since we are interested in modeling the HMXB contributions, we focus on the SFR independent component $B(L)$ (see Equation (3)). We rearrange Equation (5) to separate $B(L)$ from the rest of Δn as follows:

$$\Delta n = B(L) \cdot C_1(L) + C_2(L) \quad (6)$$

where

$$C_1(L) = \Delta L \sum_i^{N_{\mathrm{gal}}} \xi_i(L) \cdot \mathrm{SFR}_i \quad (7)$$

$$C_2(L) = \Delta L \sum_i^{N_{\mathrm{gal}}} \xi_i(L) \left[\frac{dN_{\mathrm{LMXB},i}}{dL} + \mathrm{CXB}_i(L) \right] \quad (8)$$

Note again that $B(L)$, which is scaled by the SFR of each individual galaxy, is an underlying model across all galaxies. $C_1(L)$ and $C_2(L)$ are components that scale with SFR, projected area, and stellar mass. Since these components do not contain fitting parameters, we can tabulate the values of $C_1(L)$ and $C_2(L)$ as a function of luminosity bins and fit for $B(L)$.

5. Luminosity Function Fits

In this section, we provide information on how we fit the compound model, discussed in Section 4.4, to the observed luminosity functions of subsamples of the final sample (see Section 2.3). We summarize our results and compare them to past models in Section 5.5.

5.1. Metallicity Dependence of Luminosity Function

The subsamples of the final sample are differentiated based on two factors: (1) metallicity bins with 12 + log(O/H) values of 7.7–8.3 (low), 8.3–8.9 (high) and 7.7–8.9 (full), and (2) whether the subsample contained galaxies that were targeted for ULXs. Figure 4 shows the observed X-ray luminosity functions for the resulting five unique subsamples.[4]

[4] The 8.3–8.9 metallicity bin does not contain any galaxies that were specifically targeted for ULXs.

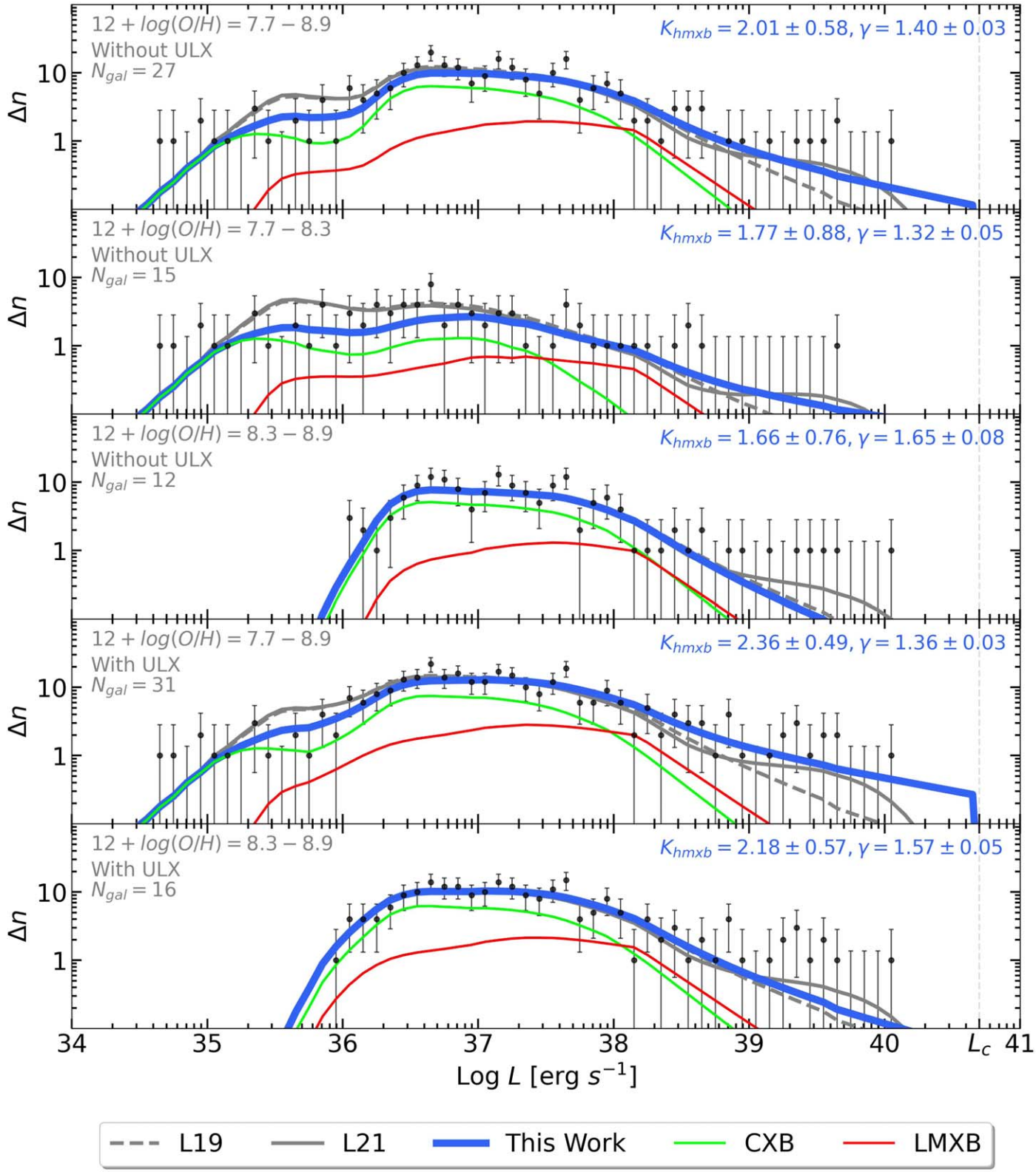

Figure 4. This figure shows models that were fit to data in three gas-phase metallicity bins. All panels show the mass and distance filtered final sample of galaxies. The first three panels show samples without galaxies that were targeted for ULXs, while the last two include them. The metallicity range and the number of galaxies in each panel are given in the upper left corner. The first and fourth panels represent the entire dwarf sample within the metallicity range of this study (i.e., 12, +,log(O/H) = 7.7 − 8.9). Observed distributions of X-ray point-source luminosities ($\Delta n = dN/dL$) for galaxy subsamples are plotted with 1σ Poisson error bars (black). Recovery functions have been applied to all models to match the expected completeness of the data. The red and green lines model LMXB and CXB contributions, respectively. The gray dashed, solid lines, and blue lines show the outputs of the combined (HMXB+LMXB+CXB) models for L19 and L21, our study. The numeric values of the fitted amplitude ($K_{\rm HMXB}$) and slope (γ) are given in the top right corner of each panel.

Table 3
Model Parameters and Goodness of Fit Tests

12 + log[O/H] Bin (1)	K_{HMXB} (2)	γ (3)	C (4)	C_{exp} (5)	C_{var} (6)	P_{null} (7)	$P_{null,L19}$ (8)	$P_{null,L21}$ (9)
7.7–8.9	2.02 ± 0.57	1.40 ± 0.03	71	61	100	0.316	0.013	0.05
7.7–8.3	1.77 ± 0.88	1.32 ± 0.05	54	57	90	0.786	0.383	0.435
8.3–8.9	1.66 ± 0.77	1.65 ± 0.08	53	40	74	0.107	0.324	0.739
7.7–8.9 (+ULX)	2.36 ± 0.49	1.36 ± 0.03	64	64	105	0.982	>0.001	0.023
8.3–8.9 (+ULX)	2.18 ± 0.57	1.57 ± 0.05	53	47	83	0.53	0.138	0.739

Note. Column (1): gas-phase metallicity. Columns (2) and (3): the values of the model parameters obtained after fitting. (4) Cash statistics value for fitted parameters. Columns (5) and (6): expected value and variance of the Cash statistics for the fitted model. Column (7): null hypothesis probability for the fitted model. Columns (8) and (9): null hypothesis probability for the L19 and L21 models.

5.2. Observed X-Ray Luminosity Functions

The observed X-ray luminosity functions are constructed by aggregating the luminosities of all X-ray point sources within all galaxy apertures in a given metallicity bin. X-ray point-source luminosities are binned into intervals similar to those in L21. The luminosity bins range from $\log L(\mathrm{erg\ s^{-1}}) = 35$–$41.7$, and each bin spans 0.1 dex, resulting in 78 bins. When inferring models, the log midpoints of the bins are used. The final sample luminosity functions for each metallicity bin are plotted as black points with error bars in Figure 4. The 1σ Poisson errors for the number of sources in each luminosity bin are calculated according to Gehrels (1986).

5.3. Model Fitting

As discussed above, the observed luminosity function for each subsample is constructed by consolidating all X-ray point sources in all galaxies within a metallicity bin. For each metallicity bin, we limit the range of L that we fit to the highest and lowest L bins that contain at least a single source. We initialize the compound model discussed in Section 4.4 using the full sample parameter values in L19 and fix the value of L_c to $10^{40.7}$ erg s^{-1}. The values of $C_1(L)$ and $C_2(L)$ are tabulated at the midpoint of each luminosity bin. We use a Levenberg–Marquardt algorithm (Astropy's `LevMarLSQFitter`) to fit K_{HMXB} and γ, which are parameters of $B(L)$, in the compound model (see Equations (3)–(5)). The quality of our models' representation of the data was evaluated using the C-statistic, as described in Section 5.4.

We account for the uncertainties in SFR by implementing a Monte Carlo sampling technique, which consists of 10^4 iterations. In each iteration, the luminosity function is refit with the SFR for each galaxy drawn from a normal distribution of SFR with a mean equal to the measured SFR and a standard deviation equal to the corresponding 1σ error. If the galaxy does not have FUV SFR measurements, we use half the SFR value as the standard deviation to reflect the relatively higher degree of uncertainty. We limit the range of allowed SFRs to 5 standard deviations from the mean and enforce a minimum SFR of 0.0001. The mean of the parameters resulting from all the iterations is taken as our final result. It is worth mentioning that the fluctuations in the SFR do not result in substantial propagated uncertainties in the fitted parameters. The parameter errors of each fit (at each iteration) are estimated by taking the diagonal of the covariance matrix from the Levenberg–Marquardt optimizer for the best SFR.

Consistent with L19, we adopt a cutoff luminosity (L_c) from their comprehensive sample fit. However, it is worth noting that this cutoff luminosity, while empirically motivated, may have significant uncertainty. This choice of fixed L_c could bias our fit. Thus, to validate its impact, we conduct a test to estimate the number of sources that our best fit predicts above this cutoff. We integrate the fitted luminosity functions above L_c and find that two or fewer sources are expected. This negligible result alleviates concerns about our fit converging on an unphysically flat slope due to artificial truncation.

5.4. Goodness of Fit

Following L19, we evaluated the goodness of fit for each of the metallicity bins on a global basis using a modified C-statistic (Cash 1979; Kaastra 2017):

$$C = 2\sum_{i=1}^{n_b} M_i - N_i + N_i \ln(N_i/M_i) \tag{9}$$

where C denotes the C-statistic corresponding to a particular metallicity bin. The sum of the statistic is calculated by iterating through the luminosity bins. n_b is the total number of luminosity bins, whereas M_i and N_i represent the model value and the observed counts for the ith bin, respectively. We mask out bins where the model is equal to zero ($C_i = 0$ if $M_i = 0$). For bins in which the observed number of sources is zero, we set the logarithmic component to zero for that term ($N_i \ln(N_i/M_i) = 0$ if $N_i = 0$).

We adopted the methods outlined by Kaastra (2017) to compute the expected C-statistic (C_{exp}), along with its variance (C_{var}), based on Poisson statistics. Subsequently, we evaluated the null hypothesis probability (P_{null}) as follows:

$$P_{null} = 1 - \mathrm{erf}\left(\sqrt{\frac{(C - C_{exp})^2}{C_{var}}}\right) \tag{10}$$

where P_{null} is the null hypothesis probability, C is the C-statistic measured from the data following Equation (9), and erf is the error function. Models with $P_{null} < 0.001$ can be statistically rejected with greater than 99.9% confidence. Utilizing a modified C-statistic, we assess the goodness of fit across various metallicity bins, and this threshold ensures the reliability of the models we test.

5.5. Fitting Results and Comparisons

The results of our fits are summarized in Table 3, and the corresponding figures are presented in Figures 4 and 5. The differential number counts of X-ray point sources as a function

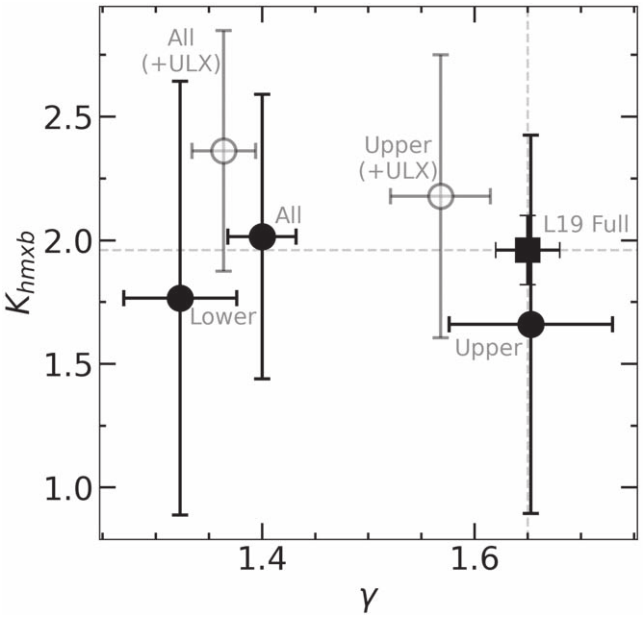

Figure 5. Parameter fits and associated 1σ errors for five subsamples compared to the L19 parameters. The square marker denotes the L19 fitted parameters and 1σ errors for their full sample. The gray dashed lines mark the L19 parameter values to help with comparison. Our subsamples without ULX galaxies are marked with filled circles, while subsamples with ULX galaxies are marked with empty circles. The metallicity bins of the subsamples are labeled by name, where all = 7.7–8.9, lower = 7.7–8.3, and upper = 8.3–8.9.

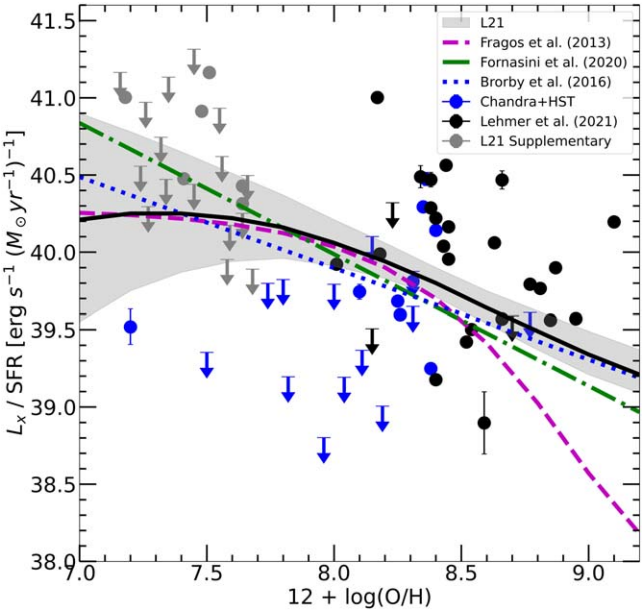

Figure 6. L_X/SFR (HMXB) vs. metallicity relation for galaxies in the Chandra +HST and all L21 samples. Dwarfs from the Chandra+HST sample are plotted in blue, and L21 galaxies are plotted in black. Galaxies from the L21 supplemental sample, which are compact dwarfs, are plotted in gray. The total HMXB L_X values are calculated by summing the observed Lx and subtracting out the LMXB and CXB contributions after correcting for completeness. Upper limits are used for galaxies with few or no sources using the expected LMXB and CXB contributions.

of luminosity are provided in Figure 4, grouped as described previously, and the best-fit parameters for the luminosity function models are provided in Figure 5.

Our analysis of the full metallicity bin reveals a power-law slope of $\gamma = 1.40 \pm 0.03$. When fitting the same metallicity bin, including galaxies targeted for ULXs, we find a slightly shallower power-law slope of $\gamma = 1.36 \pm 0.09$. However, this difference is not statistically significant, indicating that the presence of ULX-targeted galaxies does not have a meaningful effect on the overall slope of the dwarf HMXB population.

We examine the metallicity dependence of the HMXB luminosity function by fitting and comparing subsamples of galaxies binned by metallicity ranges (Section 5.1). We find that the low-metallicity bin is best fit by a shallower slope than the full sample, while the high-metallicity bin results in a steeper slope. The shallower slope of the low metallicity bin implies a relative excess of high-luminosity sources in that bin. Interestingly, only the higher metallicity bin includes ULX-targeted galaxies. Similar to the full metallicity sample, ULX-targeted galaxies in the high metallicity sample have slightly shallower luminosity function slopes, but the difference is not statistically significant. An unbiased sample is likely to provide results that lie somewhere between the ULX-included and ULX-excluded sample results.

In Figure 5, we compare the best-fit parameters to the L19 results, which utilize a broader range of stellar masses, inclusive of galaxies larger than dwarfs. We find that dwarf galaxies exhibit a shallower slope of $\gamma \sim 1.40$ compared with the full L19 sample, 1.65 ± 0.03, equating to an $\sim 8.0\sigma$ deviation, suggestive of a mass and/or metallicity dependence on the power-law slope. By contrast, we find no evidence of a dependence on the normalization parameter $K_{\rm HMXB}$. We also note that the systematic offsets in the normalization parameter due to differences in SFR measurements are found to be minimal. Specifically, the average ratio of our measurements to those in L21 is 1.07, with a standard deviation of 0.5, with a maximum deviation of ~ 2.4. We test how well these models describe the HMXB population by taking into consideration the null hypothesis probability derived from their C-stats. We find that all models result in acceptable fits, with the exception of the L19 model in the case of the full metallicity bin with ULX galaxies.

5.6. *Observed* L_X*/SFR*

In addition to looking at the luminosity function for XRBs across all the galaxies in the sample, we can also explore how the X-ray luminosity from individual sources varies with the gas-phase metallicity. Since we know that SFR is the primary driver of the L_X from HMXBs, we must normalize each L_X by the SFR in that galaxy in order to isolate any additional correlation with metallicity.

We consider L_X/SFR as a function of metallicity for individual galaxies in Figure 6. For each galaxy in the Chandra+HST sample, the total HMXB X-ray luminosity is computed by summing the observed point-source luminosities and subtracting the expected LMXB and CXB contributions. The galaxies with L_X below the expected LMXB and CXB contributions have upper limits that are 3σ above the expected background from these two sources in that galaxy.

With our expanded sample of dwarf galaxies, the vast majority of low-mass systems fall well below the predicted L_X/SFR relations. These low L_X/SFR values cannot be explained by incompleteness or aperture effects. Many of our deepest exposures have no HMXBs, and even when we double our SFR apertures, we recover the same result. As we will discuss in the next section, this wide range in L_X/SFR is actually expected because at the low SFR of the dwarfs in the Chandra+HST sample (0.01–$0.1\,M_\odot\,{\rm yr}^{-1}$), galaxies cannot

fully populate the HMXB X-ray luminosity function, and instead only a very small number of galaxies are expected to harbor a luminous XRB at any given time due to stochastic sampling (Gilfanov 2004; Lehmer et al. 2021).

6. The L_X–SFR–Metallicity Relation

We have introduced an expanded sample of dwarf galaxies with measured XRB luminosity functions, covering a broader range of sSFR and metallicity than prior work. This additional sample shows evidence for an excess of luminous X-ray sources at low metallicity in the stacked luminosity functions, and also highlights the challenges of systematic studies in dwarf galaxies where the typical SFRs are low. In order to put our results into context, we first review the theoretical reasons to expect a dependence on metallicity. We then contextualize our measured distribution of L_X/SFR with prior work.

6.1. Model Predictions

Population synthesis models (Dray 2006; Fragos et al. 2013b, 2013a; Madau & Fragos 2017) suggest that the observed scatter in the L_X–SFR relation can be explained by a secondary dependence of L_X on metallicity.

The metallicity dependence is thought to arise because stars with higher metallicity are known to undergo greater angular momentum loss due to stronger winds, which results in orbital expansion that reduces the chance of forming Roche lobe overflow (Fragos et al. 2013a). Moreover, stronger radiatively driven winds in high-metallicity stars cause them to undergo enhanced mass loss before their eventual supernova explosions (Fornasini et al. 2020). This process tends to yield compact objects that are relatively lower in mass and less numerous in high-metallicity galaxies, resulting in diminished X-ray luminosities from HMXBs. This anticorrelation causes us to expect lower-metallicity galaxies to have sources that extend to higher L_X. This trend has been seen in observations (Douna et al. 2015; Brorby et al. 2016, L19, L21), however, the same low-metallicity galaxy sample is in common across nearly all of these studies. These low-metallicity galaxies also have high specific SFRs, which correlates with low metallicity (Mannucci et al. 2010). Thus, our Chandra+HST sample both fills in intermediate metallicities and alleviates the strong bias to the highest SFRs.

6.2. SFR-driven Stochasticity

In agreement with L21, the shallower slopes observed in the stacked luminosity functions (as discussed in Section 5) imply that flatter luminosity functions are expected (i.e., more sources at higher luminosities) with decreasing metallicity. At the same time, we observe a considerable spread in L_X/SFR values for individual sources.

We can reconcile the shallower slopes in HMXB luminosity function stacks with the large spread in L_X/SFR by considering the low SFRs of the typical dwarfs in our sample. Specifically, the disparity can be largely attributed to stochastic Poissonian sampling effects that come into play due to the inherently low SFRs in dwarf galaxies. This is due to the fact that (Grimm et al. 2003; Gilfanov et al. 2004, L21)

$$L_X = \int_{L_{lo}}^{L_{up}} L\, B(L)\, dL = K_{HMXB} \int_{L_{lo}}^{L_{up}} L^{-\gamma+1} dL = \frac{K_{HMXB}}{2-\gamma}[L_{up}^{2-\gamma} - L_{lo}^{2-\gamma}] \quad (11)$$

where L_{up} and L_{lo} are the upper and lower bounds of the integrated L_X. If the power-law γ is less than 2, then the first term dominates, resulting in a highly stochastic L_X/SFR distribution through a dependence on the highest X-ray source in the galaxy. In contrast, a γ value greater than 2 results in a stable value.

Grimm et al. (2003) and L21 quantitatively explore the impact of stochasticity at low SFR. In Figure 5 of L21, they present a Monte Carlo simulation of the expected distribution in L_X/SFR given their fitted HMXB luminosity function. These simulations show an inherent stochastic scatter in L_X/SFR at low SFR and that the distributions become Gaussian at SFR $\geqslant$ 2–5 $M_\odot\,\mathrm{yr}^{-1}$, which are much higher than the typical SFR of dwarf galaxies (see Figure 1).

To quantify the spread in L_X/SFR for the Chandra+HST sample, we conducted Monte Carlo simulations utilizing the L21 HMXB luminosity function, treated as a metallicity-dependent probability density function. For each SFR and 12 + log(O/H) pairing, we initially integrated the HMXB number densities (for $\log L_X > 35$) to estimate the expected source count. Subsequently, we performed random sampling of the predicted number of HMXBs from the L21 model. This Monte Carlo approach was iterated 10,000 times, and the mean L_X/SFR for each SFR and 12 + log(O/H) pair was computed to characterize the distribution. We show the resulting probability distributions in Figure 7. The six panels correspond to SFRs of 0.005, 0.015, 0.05, 0.5, 1.0, and 5.0 $M_\odot\,\mathrm{yr}^{-1}$, respectively. We overplot the galaxies in Figure 6 binned by SFR for reference.

In Figure 7, for the lowest SFR bin (SFR = 0.005), we observe a reduced probability of detecting a galaxy with a high L_X/SFR, a consequence of stochastic Poissonian sampling, despite the over-representation of high L_X sources in the HMXB luminosity function at low metallicity 12 + log(O/H). This is because, in the case of SFR = 0.005, we expect small source number counts ($N = 2$ sources), which results in near-zero high-luminosity sources populating and dominating the total L_X of the galaxy, thereby inducing substantial stochastic variability in L_X/SFR. As the SFR increases (SFR = 0.015 and 0.05), the probability of encountering a high L_X/SFR galaxy is enhanced because of the slightly larger number of sources being sampled from the luminosity functions. If we take a slice at a low 12 + log(O/H) value (vertically) for these SFRs, the L_X/SFR probability would be a bimodal distribution due to a single source dominating the L_X of the galaxy. At high SFRs (SFR > 1.0), the larger source number counts result in the distributions becoming Gaussian, which in turn results in the probabilities approaching the L21 predictions. Thus, at high SFR, the L_X/SFR approaches the theoretical value with small scatter. The Prestwich et al. (2013) dwarf sample (L21 supplementary material) exhibits higher L_X/SFR because they have much higher specific SFR in general. In particular, six galaxies (30% of the supplementary sample) have log L_X/SFR above 40 and SFRs that are greater than 0.01.

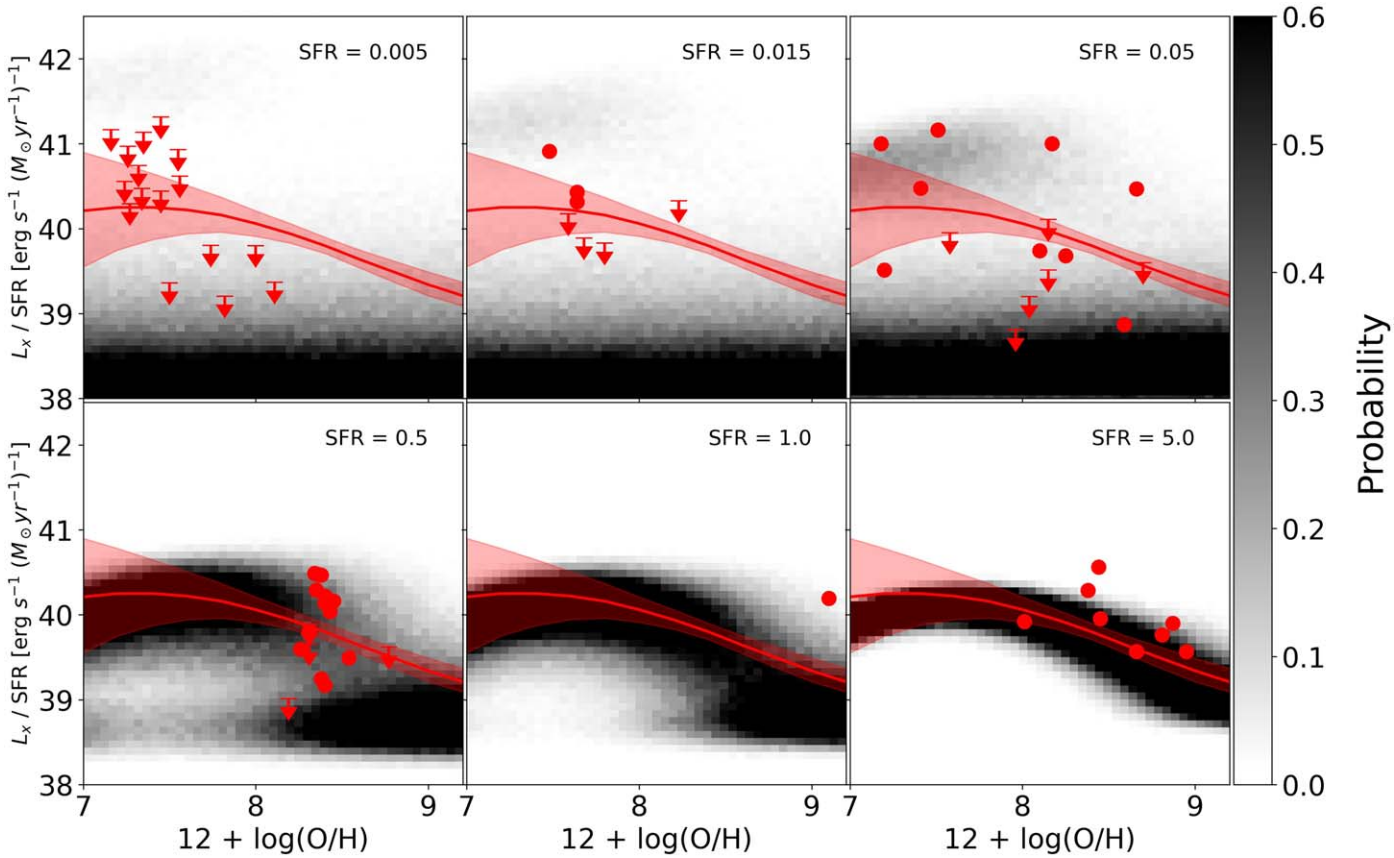

Figure 7. We show the probabilistic distribution of L_X/SFR against 12 + log(O/H) for SFRs and gas-phase metallicities similar to the dwarf samples discussed in this work. The Monte Carlo probabilities were computed for each SFR and 12 + log(O/H) pair by using the L21 HMXB model as the probability density function. The six panels correspond to SFRs of 0.005, 0.015, 0.05, 0.5, 1.0, and 5.0 $M_\odot$ yr^{-1}, respectively. The grayscale shows the probability of finding a galaxy with an L_X/SFR for a given 12 + log(O/H). The red markers show the observed galaxy L_X/SFR values and upper limits, including all galaxies in this work and L21 for reference (not just dwarfs). The red line represents the L21 model prediction for reference. At lower SFRs, the probability of encountering a high L_X/SFR galaxy is reduced due to stochastic Poissonian sampling, despite a surplus of high L_X sources in the HMXB luminosity function of galaxies with low 12 + log(O/H). With increasing SFR, the probability distribution approaches the L21 prediction (red line). Some observed points may hover slightly above or below the probability evaluated at the SFR displayed, this is due to the scatter introduced by the range of galaxy SFRs.

Returning to one of our main motivations for this work, to understand how and when we may use L_X/SFR to search for accreting massive black holes, we have a hopeful message. While it will be necessary to fold in the detailed SFR distributions and (ideally) metallicity distributions for a sample to derive the expected number of detections from HMXBs alone, these distributions mean that the contribution from HMXBs should be low (∼3%–4%) from dwarfs that lie on the star-forming main sequence and the local mass–metallicity relation.

7. Summary

In this paper, we present the HMXB X-ray luminosity functions of dwarf galaxies within the Local Volume, and specifically investigate the role of metallicity in setting the HMXB luminosity function.

1. We introduce the Chandra+HST sample, a selection of local volume dwarf galaxies drawn from the LEGUS and STARBIRDS data sets. These galaxies have multiband coverage provided by HST, GALEX, IRAC, and Chandra. Combined with 11 local dwarfs from L21, we present a total sample of 35 dwarf galaxies spanning a stellar mass range of (log $M_*/M_\odot$) 6.8–9.52, gas-phase metallicity (12 + log(O/H)) range of 7.74–8.77, and a distance range of 0.5–12 Mpc. The Chandra+HST sample presented here effectively complements the L21 sample by bridging the metallicity gap between their main and supplementary subsamples, while sampling a wider range of sSFR.
2. We model the HMXB X-ray luminosity functions of local dwarf galaxies across a luminosity range of $\log L = 34.1$–41.7 and a metallicity range of 12 + log(O/H) = 7.7–8.9. We find that the power-law slope of the luminosity function is shallower (above 3σ) for our local sample compared to the L19 full sample, which consists of more massive galaxies with higher metallicities.
3. After dividing our final sample into two metallicity bins, we observe that the lower-metallicity bin exhibits a shallower power-law slope, which suggests a relative excess of high L_X sources as a function of metallicity. This result holds regardless of whether we include or exclude galaxies that were initially targeted for harboring ULXs.
4. We observe a large spread in L_X/SFR for galaxies in the Chandra+HST sample. We attribute this deviation to the Poissonian sampling of the luminosity functions that is caused by the relatively lower sSFRs of dwarf galaxies.

In addition to our results, we expect that SFHs and galaxy concentration significantly influence the HMXB luminosity

distribution and sampling of HMXBs in dwarf galaxies. In particular, galaxies with recent SFHs that deviate from the average dwarf population are prime candidates for further study. Galaxy concentration could potentially introduce variations in the luminosity function of HMXBs due to differences in binary system formation rates, enhanced stellar interactions, and the influence of stellar evolution within densely concentrated regions. Lastly, a larger sample of dwarf galaxies would help in constraining the high $\log L_X/\mathrm{SFR} > 40$ regime for the sSFR range explored in this study.

Acknowledgments

R.G. and A.D.G. acknowledge funding provided by the National Aeronautics and Space Administration through Chandra award No. AR2-23011X granted by the Chandra X-ray Center, which is operated by the Smithsonian Astrophysical Observatory for and on behalf of the National Aeronautics Space Administration under contract NAS8-03060. J.E.G. acknowledges support from National Science Foundation award Nos. AAG/1007052 and AAG/1007094. B.D.L. acknowledges support from the Astrophysics Data Analysis Program (ADAP) 80NSSC20K0444. This research has made use of new data obtained by the Chandra X-ray Observatory and data obtained from the Chandra Data Archive, as well as software provided by the Chandra X-ray Center (CXC). We would also like to thank our reviewer for the insightful comments and suggestions.

Software: CIAO (Fruscione et al. 2006) Astropy (Astropy Collaboration et al. 2022), SciPy (Virtanen et al. 2020), NumPy (Harris et al. 2020), matplotlib (Hunter 2007),

Appendix

In Table 4, we present a table of point sources within the apertures of the Chandra+HST sample.

Table 4
An Abbreviated Version of the Source Catalog for the Chandra+HST Sample

Name	α_{J2000} R.A.	δ_{J2000} Decl.	$N_{0.5-7\ \mathrm{keV}}$ Counts	$\mathrm{Log}F_{0.5-7\mathrm{keV}}$ (log erg cm^{-2} s^{-1})
(1)	(2)	(3)	(4)	(5)
NGC 0045	$00^h14^m03^s.0$	−23°12′19.″1	80.41 ± 12.43	−14.041
	$00^h14^m03^s.6$	−23°10′07.″1	53.38 ± 8.97	−14.219
	$00^h14^m06^s.1$	−23°10′05.″8	58.29 ± 7.31	−14.181
	$00^h14^m11^s.5$	−23°11′38.″5	3.26 ± 7.63	−15.434
	$00^h14^m04^s.0$	−23°10′55.″5	13.28 ± 1.80	−14.823
	$00^h13^m58^s.3$	−23°11′07.″3	16.58 ± 3.64	−14.727
	$00^h14^m00^s.9$	−23°10′17.″0	6.78 ± 3.30	−15.116
	$00^h14^m01^s.2$	−23°08′28.″0	14.83 ± 5.57	−14.776
NGC 0625	$01^h35^m03^s.5$	−41°26′14.″2	296.07 ± 17.21	−13.718
	$01^h35^m07^s.1$	−41°26′05.″4	607.84 ± 24.65	−13.405
	$01^h35^m07^s.3$	−41°26′11.″2	16.79 ± 3.83	−14.964
NGC 1313	$03^h18^m07^s.2$	−66°30′46.″0	4.27 ± 9.02	−15.243
	$03^h18^m06^s.4$	−66°30′38.″6	55.67 ± 4.86	−14.128
	$03^h18^m05^s.5$	−66°30′14.″9	149.06 ± 17.19	−13.701
	$03^h18^m18^s.2$	−66°30′04.″2	365.14 ± 2.07	−13.312
	$03^h18^m18^s.9$	−66°30′01.″5	286.30 ± 7.46	−13.417
	$03^h18^m20^s.0$	−66°29′11.″1	5241.10 ± 12.21	−12.155
	$03^h18^m29^s.5$	−66°28′41.″2	9.88 ± 19.11	−14.879
	$03^h18^m23^s.7$	−66°28′34.″6	16.56 ± 16.92	−14.655
	$03^h18^m21^s.2$	−66°28′58.″6	13.40 ± 72.40	−14.747

Note. The full catalog contains 184 sources, and a description is provided in the appendix. The full table contains the following columns: Column (1): name of the galaxy that the source belongs to. Columns (2) and (3): R.A. and decl. of the point source. Column (4): 0.5–7 keV net counts and 1σ errors. Column (5): 0.5–7 flux of the source.

(This table is available in its entirety in machine-readable form.)

ORCID iDs

Robel Geda https://orcid.org/0000-0003-1509-9966
Andy D. Goulding https://orcid.org/0000-0003-4700-663X
Bret D. Lehmer https://orcid.org/0000-0003-2192-3296
Jenny E. Greene https://orcid.org/0000-0002-5612-3427
Anish Kulkarni https://orcid.org/0000-0002-8477-7137

References

Abbott, B. P., Abbott, R., Abbott, T. D., et al. 2016, ApJL, 818, L22
Astropy Collaboration, Price-Whelan, A. M., Lim, P. L., et al. 2022, ApJ, 935, 167
Barrow, K. S. S., Wise, J. H., Aykutalp, A., et al. 2018, MNRAS, 474, 2617
Basu-Zych, A. R., Lehmer, B., Fragos, T., et al. 2016, ApJ, 818, 140
Basu-Zych, A. R., Lehmer, B. D., Hornschemeier, A. E., et al. 2013, ApJ, 762, 45
Bell, E. F., & de Jong, R. S. 2001, ApJ, 550, 212
Bothwell, M. S., Kennicutt, R. C., & Lee, J. C. 2009, MNRAS, 400, 154
Brorby, M., Kaaret, P., & Prestwich, A. 2014, MNRAS, 441, 2346
Brorby, M., Kaaret, P., & Prestwich, A. 2016, MNRAS, 457, 4081
Calzetti, D., Lee, J. C., Sabbi, E., et al. 2015, AJ, 149, 51
Cash, W. 1979, ApJ, 228, 939
Cignoni, M., Sacchi, E., Aloisi, A., et al. 2018, ApJ, 856, 62
Cignoni, M., Sacchi, E., Tosi, M., et al. 2019, ApJ, 887, 112
Douna, V. M., Pellizza, L. J., Mirabel, I. F., & Pedrosa, S. E. 2015, A&A, 579, A44
Dray, L. M. 2006, MNRAS, 370, 2079
Eide, M. B., Graziani, L., Ciardi, B., et al. 2018, MNRAS, 476, 1174
Fornasini, F. M., Civano, F., Fabbiano, G., et al. 2018, ApJ, 865, 43
Fornasini, F. M., Civano, F., & Suh, H. 2020, MNRAS, 495, 771
Fragos, T., Lehmer, B., Tremmel, M., et al. 2013a, ApJ, 764, 41
Fragos, T., Lehmer, B. D., Naoz, S., Zezas, A., & Basu-Zych, A. 2013b, ApJL, 776, L31
Fruscione, A., McDowell, J. C., Allen, G. E., et al. 2006, Proc. SPIE, 6270, 62701V
Gehrels, N. 1986, ApJ, 303, 336
Gilfanov, M. 2004, MNRAS, 349, 146
Gilfanov, M., Grimm, H. J., & Sunyaev, R. 2004, MNRAS, 351, 1365
Greene, J. E., Strader, J., & Ho, L. C. 2020, ARA&A, 58, 257
Grimm, H. J., Gilfanov, M., & Sunyaev, R. 2003, MNRAS, 339, 793
Haiman, Z., Brandt, W. N., Vikhlinin, A., et al. 2019, BAAS, 51, 557
Halevi, G., Goulding, A., Greene, J., et al. 2019, ApJL, 885, L3
Harris, C. R., Millman, K. J., van der Walt, S. J., et al. 2020, Natur, 585, 357
Hornschemeier, A. E., Brandt, W. N., Garmire, G. P., et al. 2000, ApJ, 541, 49
Hunter, J. D. 2007, CSE, 9, 90
Jarrett, T. H., Chester, T., Cutri, R., Schneider, S. E., & Huchra, J. P. 2003, AJ, 125, 525
Kaastra, J. S. 2017, A&A, 605, A51
Kim, D. W., Cameron, R. A., Drake, J. J., et al. 2004, ApJS, 150, 19
Kim, M., Wilkes, B. J., Kim, D.-W., et al. 2007, ApJ, 659, 29
Kovlakas, K., Zezas, A., Andrews, J. J., et al. 2020, MNRAS, 498, 4790
Lee, J. C., Gil de Paz, A., Tremonti, C., et al. 2009, ApJ, 706, 599
Lehmer, B. D., Alexander, D. M., Bauer, F. E., et al. 2010, ApJ, 724, 559
Lehmer, B. D., Basu-Zych, A. R., Mineo, S., et al. 2016, ApJ, 825, 7
Lehmer, B. D., Eufrasio, R. T., Basu-Zych, A., et al. 2021, ApJ, 907, 17
Lehmer, B. D., Eufrasio, R. T., Tzanavaris, P., et al. 2019, ApJS, 243, 3
Liotine, C., Zevin, M., Berry, C. P. L., Doctor, Z., & Kalogera, V. 2023, ApJ, 946, 4
Madau, P., & Fragos, T. 2017, ApJ, 840, 39
Mannucci, F., Cresci, G., Maiolino, R., Marconi, A., & Gnerucci, A. 2010, MNRAS, 408, 2115
Mapelli, M., Ripamonti, E., Zampieri, L., Colpi, M., & Bressan, A. 2010, MNRAS, 408, 234
Martin, D. C., Fanson, J., Schiminovich, D., et al. 2005, ApJL, 619, L1
McQuinn, K. B. W., Mitchell, N. P., & Skillman, E. D. 2015, ApJS, 218, 29
McQuinn, K. B. W., Skillman, E. D., Cannon, J. M., et al. 2010, ApJ, 724, 49
Mezcua, M. 2017, IJMPD, 26, 1730021
Mezcua, M., Civano, F., Marchesi, S., et al. 2018, MNRAS, 478, 2576
Mineo, S., Gilfanov, M., & Sunyaev, R. 2012, MNRAS, 419, 2095
Natarajan, P., Pacucci, F., Ferrara, A., et al. 2017, ApJ, 838, 117
Pardo, K., Goulding, A. D., Greene, J. E., et al. 2016, ApJ, 831, 203
Persic, M., Rephaeli, Y., Braito, V., et al. 2004, A&A, 419, 849
Podsiadlowski, P., Rappaport, S., & Han, Z. 2003, MNRAS, 341, 385
Ponnada, S., Brorby, M., & Kaaret, P. 2020, MNRAS, 491, 3606
Prestwich, A. H., Tsantaki, M., Zezas, A., et al. 2013, ApJ, 769, 92
Ranalli, P., Comastri, A., & Setti, G. 2003, A&A, 399, 39
Ricarte, A., & Natarajan, P. 2018, MNRAS, 481, 3278
Rosati, P., Tozzi, P., Giacconi, R., et al. 2002, ApJ, 566, 667
Sacchi, E., Cignoni, M., Aloisi, A., et al. 2018, ApJ, 857, 63
Saxena, A., Ellis, R. S., Förster, P. U., et al. 2021, MNRAS, 505, 4798
Schlegel, D. J., Finkbeiner, D. P., & Davis, M. 1998, ApJ, 500, 525
Schramm, M., Silverman, J. D., Greene, J. E., et al. 2013, ApJ, 773, 150
Skrutskie, M. F., Cutri, R. M., Stiening, R., et al. 2006, AJ, 131, 1163
Tremonti, C. A., Heckman, T. M., Kauffmann, G., et al. 2004, ApJ, 613, 898
Virtanen, P., Gommers, R., Oliphant, T. E., et al. 2020, NatMe, 17, 261
Warszawski, L., Geil, P. M., & Wyithe, J. S. B. 2009, MNRAS, 396, 1106